Estimation of Host Rock Thermal Conductivities Using the Temperature Data From the Drift Scale Test at Yucca Mountain, Nevada

S. Mukhopadhyay and Y. W. Tsang
Ernest Orlando Lawrence Berkeley National Laboratory, Berkeley, California

Abstract

A large volume of temperature data has been collected from a very large, underground heater test, the Drift Scale Test (DST) at Yucca Mountain, Nevada. The DST was designed to obtain thermal, hydrological, mechanical, and chemical (THMC) data in the unsaturated fractured rock of Yucca Mountain. Sophisticated numerical models have been developed to analyze the collected THMC data. In these analyses, thermal conductivities measured from core samples have been used as input parameters to the model. However, it was not known whether these core measurements represented the true field-scale thermal conductivity of the host rock. Realizing these difficulties, elaborate, computationally intensive geostatistical simulations have also been performed to obtain field-scale thermal conductivity of the host rock from the core measurements. In this paper, we use the temperature data from the DST as the input (instead of the measured core-scale thermal conductivity values) to develop an estimate of the field-scale thermal conductivity values. Assuming a conductive thermal regime, we develop an analytical solution for the temperature rise in the host rock of the DST; and using a nonlinear fitting routine, we obtain a best-fit estimate of field-scale thermal conductivity for the DST host rock. The temperature data collected from the DST shows clear evidence of two distinct thermal regimes: a zone below boiling (wet) and a zone above boiling (dry). We obtain estimates of thermal conductivity for both the wet and dry zones. We also analyze the sensitivity of these estimates to the input heating power of the DST.

Gap numbers: 1829 Groundwater hydrology; 1832 Groundwater transport; 1875 Unsaturated zone

1. Introduction

The Drift Scale Test (DST), located in the Topopah Spring middle nonlithophysal (Tptpmn) stratigraphic unit of Yucca Mountain, Nevada, is the largest ever *in situ* heater test conducted in fractured welded tuff. The DST was designed to investigate the coupled thermal-hydrological-mechanical-chemical (THMC) changes in the host rock caused by long-term heating. Data collected from the DST are assisting the scientists and engineers to develop an understanding of the THMC changes likely to be encountered in the host rock around the high-level radioactive waste repository at Yucca Mountain. A more detailed discussion about the DST and analyses of the thermal-hydrological (TH) changes arising out of the DST can be found in *Birkholzer and Tsang* [2000] and *Mukhopadhyay and Tsang* [2003] and references therein.

In the DST, heating was continuously provided by electrical heaters for slightly more than four years. During this heating phase, a substantial volume (more than 100,000 m^3) of rock experienced a significant increase in temperature, along with associated THMC changes. An elaborate active and passive data collection system allowed recording of these THMC changes (including temperature rise) in the rock. The objective of this paper is to utilize the temperature data from the DST for estimating the thermal conductivities of the host rock. Given the large volume of the host rock heated during the DST, it is reasonable to expect that thermal conductivities estimated in such a manner would reflect field-scale thermal conductivities of the DST host rock. These estimated field-scale thermal properties are thus expected to be more useful in predicting the long-term THMC conditions in the vicinity of the repository than laboratory measurements.

The fractured welded tuff surrounding the DST has an ambient, preheating matrix water saturation of approximately 90% [*Tsang et al*., 1999]. In other words, the rock matrix is considerably "wet" under ambient conditions. During the early phases of heating in the DST, heat transfer occurred through this wet rock. With continued heating, as the temperature approached boiling near the source of heat, some of this pore water was converted to vapor, which then moved away from the source of heating and condensed in the cooler parts of the rock. The condensate above the heat source thereafter started flowing back towards it under gravity drainage. This countercurrent flow of vapor and condensate gave rise to coupling of thermal and hydrological processes and resulted in what could be called "heat-pipe" signatures, a flat zone in a temperature vs. time plot. The temperature data collected from the DST showed ample evidence of these heat-pipe signatures [*Birkholzer and Tsang*, 2000; *Mukhopadhyay and Tsang*, 2003]. With further heating and boiling of pore water, a "dryout" zone was formed in the host rock in the immediate vicinity of the heat source.

In the later stages of heating, therefore, heat transfer occurred in three distinct regimes. In the vicinity of the HD and the wing heaters, heat transfer occurred through the dry rock. At the same time, far away from the heat sources, heat transfer was still happening on account of the wet rock. In between these two regimes, was a two-phase regime, where most of the boiling was taking place. These three regimes are clearly visible in the DST temperature data discuss later (Section 3). Although the transformation from the wet to the dry rock scenario is a dynamic process, through careful analysis of the temperature data, it is possible to estimate wet and dry thermal conductivities of the rock. Because the host rock, after emplacement of radioactive wastes, is expected to experience similar "wet" and "dry" conditions, it may be useful to estimate these wet and dry thermal conductivities from actual temperature changes in the rock.

It needs to be emphasized that overall temperature rise in the host rock of the DST is actually the outcome of coupling between thermal and hydrological processes. These

processes include heat conduction through the rock, fluid migration (movement of water and vapor as described above), phase changes, radiative heat transport, and natural convection. Of these processes, heat conduction is considered to be one of the dominant transport mechanisms and is essentially controlled by the thermal conductivity (k) of the surrounding rock. In a conductive heat-transfer regime, in addition to k, another parameter plays a significant role in determining the transient temperature profile in the rock. This is the thermal diffusivity (α) of the rock.

Sophisticated numerical models have been developed to analyze the temperature data from the DST [*Birkholzer and Tsang*, 2000; *Civilian Radioactive Waste Management Systems*, *CRWMS*, 2000; *Mukhopadhyay and Tsang*, 2003; *Birkholzer et al.*, 2003, and references therein]. For these numerical models, representative values of k and α of the host rock are provided as input. These input parameters have their origin in laboratory measurements of thermal properties of cores collected from various boreholes near the location of the DST (*Brodsky et al*., 1997). The measured thermal conductivity values (*Brodsky et al*., 1997) have a wide range and spatial variability. Note also that reliable measured thermal conductivity data are limited. Under these constraints, the estimation of representative host rock k and α values is difficult.

Ramsey et al. (2002) recognized these difficulties in determining a mean thermal conductivity value. In response, they started with a three-dimensional cubic model (*Hsu et al*., 1995) for thermal conductivity of a porous medium. In this model, overall thermal conductivity is a function of the porosity, the thermal conductivity of the fluid in the pore space, the thermal conductivity of the solid, and the geometry and connectivity of the solid. Ramsey et al. (2002) treated the thermal conductivity of the fluid as constant but the remaining model parameters were treated as spatially uncertain random functions. They then employed sequential Gaussian simulation to develop 50 equally likely realizations of those uncertain parameters. Thermal conductivity measurments of Brodsky et al. (1997) and petrophysical measurements (for porosity) were used to condition these uncertain properties. Through these elaborate geostatistical simulations, they generated the spatial distribution of thermal conductivity values for various stratigraphic layers and computed the mean and standard deviation of thermal conductivity (both wet and dry) for each of those layers. These may be more reliable estimates of mean thermal conductivity values compared to the raw core measurement data. However, computational burden of the procedures adopted by Ramsey et al. (2002) may be too intensive.

In this paper, we propose to estimate thermal conductivity using the temperature data from the DST. One way of obtaining the thermal properties of the host rock from its temperature response is to employ an elaborate inverse modeling approach, using software such as the ITOUGH2 [*Finsterle*, 1999]. Such an ITOUGH2-based inverse

modeling involves many forward simulations of the complex TH processes associated with the DST. Given the complex geometry of the DST and the complexities of the physical processes, a single forward TH simulation of the DST requires close to four weeks' computation time on some of the fastest machines currently available. A full inverse modeling (which necessitates several such forward TH simulations) of the temperature data from the DST is computationally prohibitive. In the absence of complete inverse modeling, one may also adopt an approach based on selective inverse modeling of the temperature data (such as fitting temperature data from a two-dimensional slice of the three-dimensional model) to obtain an estimate of the thermal properties. However, such selective analysis is always open to debate regarding the validity of the estimated properties.

Here, we present an efficient methodology to obtain a reliable field-scale estimate of thermal conductivities. The approach is based on an analytical solution for the spatial and temporal evolution of temperature rise caused by heating at the DST. To obtain the analytical solution, we assume that the temperature rise in the rock happens entirely due to heat conduction. It is also assumed that the rock is homogeneous and isotropic. We also need to assume that no pore-water phase change takes place during heating. In the actual test, though, some part of the input energy is used in providing latent heat of vaporization for the pore water. Previous modeling experience [*Mukhopadhyay and Tsang*, 2003] with the DST has demonstrated that about 74–81% (depending upon time) of the input heat energy goes into heating the rock. Since the analytical solution is based upon a 'no-phase-change' assumption, we will use only the portion of the input energy that was used for heating rock as heat input to the analytical model. Finally, it is also assumed that the thermal properties are independent of temperature. In other words, the estimates of the thermal conductivities from the model should be construed as averaged over the appropriate temperature range. Comparing the analytical solution with the measured temperature rise at any given location and at any given time, we obtain the thermal conductivities using a nonlinear parameter estimation technique based on Gauss-Newton approach (see Section 4).

The rest of the paper is organized as follows. We begin with a brief description of the DST in Section 2. In Section 3, we present some representative temperature data collected from the DST and illustrate the various thermal regimes encountered in the DST during heating. In Section 4, we provide the analytical solution for spatial and temporal evolution of temperature rise in the host rock surrounding the host rock. We also discuss the nonlinear fitting techniques used in this section. Section 5 discusses the findings from our analysis of the temperature data. Section 6 provides a summary of methods and results.

2. Description of the DST

The DST consists of a 47.5 m long, 5 m diameter Heated Drift (HD). The HD is connected to the outside world through a bulkhead, which is used as the origin of the coordinate system in our calculations. Heating in the DST started on December 3, 1997, and ended on January 14, 2002. Heat was provided by 9 canister heaters located on the floor of the HD. Additional heating was provided by 50 wing heaters, placed orthogonal to the axis of the HD, with 25 of them on each side of the HD. Each of the wing heaters has two parts, inner wing heater and outer wing heater. The inner wing heater starts at 1.67 m from the Heated Drift and is 4.44 m long. There is a gap of 0.66 m between the inner and outer wing heater. The outer wing heater is also 4.44 m long. Temperature data from the DST were continuously collected by approximately 1,700 resistance temperature devices (RTD) placed in 26 boreholes (Borehole 133–134, 137–144, 158–165, 169–175). Each of these boreholes is collared at the wall of the Heated Drift and is approximately 20 m in length. They are oriented either vertically, horizontally, or at an angle of 45^{o} with the HD. Figure 1 shows a schematic picture of the HD, the bulkhead, the wing heaters, and the locations of the temperature data collection boreholes. A more detailed description of the DST and the data collection boreholes can be found in *CRWMS* [1998].

The total design power of the nine canister heaters was 67 kW; and that of the 50 wing heaters was 143 kW [*CRWMS*, 1998]. However, the actual heat output from these heaters varied somewhat during the course of the test (which included a few power outages). Figure 2 shows the actual total heat output from these heaters as a function of time. Starting at 27 months of heating (March 2000), power was reduced, in a series of steps, to keep the temperature at the wall of the HD at a targeted maximum of 200^{o}C. In the analysis that follows, we will use an average of the actual heat output from the heaters as the total power available for heating. Table 1 shows the calculated average of the actual heating power at different times during heating. These are the powers that have been used in our calculations. For example, for obtaining results at 36 months of heating, computations were performed using the average total heating power up to 36 months.

3. Measured Temperature Data from the DST

Figure 3a shows measured temperature data as a function of radial distance from the DST at 2 months of heating in Boreholes 137–144 (see Figure 1). Boreholes 137–144 are located about 11.9 m from the bulkhead [*CRWMS*, 1998]. The drift wall is at about 95^{o}C after 2 months of heating. Temperatures then fall rapidly with distance, except for Boreholes 139 and 143. These two boreholes are located parallel to the wing heater (see

Figure 1). Because of the gap between the HD and the inner wing heater, temperatures in this zone decline with distance in these two boreholes. Afterwards, temperatures begin to rise with distance because of the additional heat coming from the inner wing heater. At the end of the inner wing heater, temperatures drop again because of the gap between the inner and outer wing heater. Temperatures thereafter rise again with distance along the length of the outer wing heater. Beyond the end of the outer wing heater, temperatures decline with distance, as in other boreholes.

Figure 3b shows measured temperatures in the same borehole group after 48 months of heating, i.e., very close to the end of the heating phase (the total heating phase was approximately 49.5 months). The temperature profiles are similar to those described in Figure 3a, except that the temperatures are considerably higher because of the continued heating. Additionally, three distinct zones are now observable in the temperature profile. Considering Boreholes 137–138, 140–142, and 144, there is a zone of an almost linear profile with temperatures above 100°C. This zone extends 5–8 m from the wall of the HD. At the end of the first zone, there is a flat profile with temperatures around 96-97°C, indicating the presence of TH coupling (heat-pipe signatures). At the end of the flat profile, there is a third zone with (again) an almost linear decline in temperature. The slope of the temperature profile line in this zone is clearly different (larger) from the one for the first zone. This change in slope happens because heat transfer occurs through dry rock in the first zone, whereas wet rock governs heat transfer in the third zone.

We will shortly show that temperature data from these two zones can be used to obtain dry and wet thermal properties of the rock, respectively. The same patterns are also observed for Boreholes 139 and 143 if we consider the profile from the end of the wing heaters instead of the HD. Notice also that there are some differences in the temperature profiles between even symmetrically located boreholes; such differences may have resulted from local heterogeneities. Temperature profile data collected from other boreholes are similar to those shown in Figures 3a and 3b, because of the symmetry of their locations.

4. Methodology

Figure 4 presents a schematic representation of the conceptual model developed in this section. Figure 4 also shows the coordinate system for the mathematical derivations. The temperature rise ΔT (x, y, z, t) at any sensor location (x, y, z) inside the rock and at any time t can be expressed as

$$\Delta T(x, y, z, t) = \Delta T_H(x, y, z, t) + \Delta T_W(x, y, z, t), \quad (1)$$

where ΔT_H and ΔT_W are the temperature rise due to heat emanating from the HD and the wing heaters, respectively. To obtain an expression for ΔT_H, we can show that the temperature rise at location (x, y, z) inside a solid, owing to an instantaneous point source of $Q\rho C$ units of heat [*Carslaw and Jaeger*, 1959, pp. 256] at location (x_o, y_o, z_o), is

$$\Delta T_H = \frac{Q}{(4\pi\alpha t)^{\frac{3}{2}}} e^{-\frac{(x-x_o)^2+(y-y_o)^2+(z-z_o)^2}{4\alpha t}}, \tag{2}$$

where $\alpha=k/(\rho C)$. Since the HD is of length H (= 47.5 m) along the y-axis (see Figure 4), the heat source can be treated as distributed along a line of length H instead of being a point source. We can then readily write [*Carslaw and Jaeger*, 1959, pp. 258]

$$\begin{aligned} \Delta T_H &= \frac{Q}{H\ (4\pi\alpha t)^{\frac{3}{2}}} \int_0^H e^{-\frac{(x-x_o)^2+(y-y_o)^2+(z-z_o)^2}{4\alpha t}} dy_o \\ &= \frac{Q}{8\pi\alpha t H} e^{-\frac{(x-x_o)^2+(z-z_o)^2}{4\alpha t}} \left[erf\left(\frac{y}{2\sqrt{\alpha t}}\right) + erf\left(\frac{H-y}{2\sqrt{\alpha t}}\right) \right] \end{aligned}. \tag{3}$$

In Equation (3), erf (η) is the error function

$$erf(\eta) = \frac{2}{\sqrt{\pi}} \int_0^\eta e^{-\phi^2} d\phi \tag{4}$$

Assuming that the polar coordinates of the points (x, z) and (x_o, z_o) are (r, θ) and (r_o, θ_o), respectively, the heat source can now be distributed over a circle with radius r_o (= 2.5 m for the HD). Equation (3) can now be rewritten [*Carslaw and Jaeger*, 1959] as

$$\begin{aligned} \Delta T_H &= \frac{Q}{8\pi\alpha t H} \left[erf\left(\frac{y}{2\sqrt{\alpha t}}\right) + erf\left(\frac{H-y}{2\sqrt{\alpha t}}\right) \right] \left[\frac{1}{2\pi} \int_0^{2\pi} e^{-\frac{r^2+r_o^2-2rro\cos\theta_o}{4\alpha t}} d\theta_o \right] \\ &= \frac{Q}{8\pi\alpha t H} \left[erf\left(\frac{y}{2\sqrt{\alpha t}}\right) + erf\left(\frac{H-y}{2\sqrt{\alpha t}}\right) \right] I_0\left(\frac{rr_o}{2\alpha t}\right) e^{-\frac{r^2+r_o^2}{4\alpha t}} \end{aligned}, \tag{5}$$

where $r = \sqrt{(x^2 + z^2)}$ and $I_0(\eta)$ is the modified Bessel function of the first kind with order 0 and argument η. In deriving Equation (5), the following property of the modified Bessel function has been utilized [*Abramowitz and Stegun*, 1964]

$$\int_0^{2\pi} e^{\eta\cos\varphi} d\varphi = 2\pi I_0(\eta). \tag{6}$$

Since for the DST, the source of heat is a continuous one, we need to evaluate one more integral [*Carslaw and Jaeger*, 1959, pp. 261] to obtain the final expression

$$\Delta T_H = \frac{1}{8\pi\alpha H}\int_0^t \left[erf\left(\frac{y}{2\sqrt{\alpha(t-t_o)}}\right) + erf\left(\frac{H-y}{2\sqrt{\alpha(t-t_o)}}\right)\right] I_0\left[\frac{rr_o}{2\alpha(t-t_o)}\right] e^{-\frac{r^2+r_o^2}{4\alpha(t-to)}} \frac{\phi(t_o)dt_o}{t-t_o}$$

$$= \frac{J_H}{4\pi kH}\int_{\frac{1}{2\sqrt{\alpha t}}}^{\infty} \left[erf(y\tau) + erf\{(H-y)\tau\}\right] I_0\left[2rr_o\,\tau^2\right] e^{-(r^2+r_o^2)\tau^2}\frac{d\tau}{\tau} \tag{7}$$

In Equation (7), J_H is the average of the total power provided by the canister heaters. The integral in Equation (7) obviously needs to be evaluated numerically.

Similarly, the contribution to the total temperature rise from the wing heaters (ΔT_W) can be obtained. It is useful to consider the wing heaters as line sources of heat. Observe that the wing heaters are located parallel to the x-axis at various y locations. With Equation (2) as the starting point again, we can write the temperature rise resulting from the first pair of wing heaters as

$$\Delta T_{w1} = \frac{Q_W}{(1-l_o)(4\pi\alpha t)^{\frac{3}{2}}} e^{-\frac{(y-y_o)^2+(z-z_o)^2}{4\alpha t}} \left[\int_{-l}^{-lo} e^{-\frac{(x-x_o)^2}{4\alpha t}}dx_o + \int_{lo}^{l} e^{-\frac{(x-x_o)^2}{4\alpha t}}dx_o\right]. \tag{8}$$

Since there are 25 pairs of such line sources at various y-locations, the total temperature rise due to these line sources is

$$\Delta T_w = \frac{Q_W}{M(1-l_o)(4\pi\alpha t)^{\frac{3}{2}}} \sum_{m=1}^{M} e^{-\frac{(y-y_{(m)})^2+(z-z_o)^2}{4\alpha t}} \left[\int_{-l}^{-lo} e^{-\frac{(x-x_o)^2}{4\alpha t}}dx_o + \int_{lo}^{l} e^{-\frac{(x-x_o)^2}{4\alpha t}}dx_o\right]$$

$$= \frac{Q_W}{8\pi\alpha t M(1-l_o)} \sum_{m=1}^{M} e^{-\frac{(y-y_{(m)})^2+(z-z_o)^2}{4\alpha t}} \left[\begin{array}{l} erf\left(\frac{x+l}{2\sqrt{\alpha t}}\right) - erf\left(\frac{x+l_o}{2\sqrt{\alpha t}}\right) + \\ erf\left(\frac{x-l_o}{2\sqrt{\alpha t}}\right) - erf\left(\frac{x-l}{2\sqrt{\alpha t}}\right) \end{array}\right] \tag{9}$$

where M is the total pairs (= 25) of wing heaters and $y(m)$ is the distance of the m-th wing heater from the bulkhead along the y-axis. Recognizing that the heat source is continuous, we need to rewrite Equation (9) as:

$$\Delta T_w = \frac{1}{8\pi\alpha M(1-l_o)} \int_0^t \frac{\varphi(t_o)dt_o}{t-t_o} \sum_{m=1}^{M} e^{-\frac{(y-y_{(m)})^2+(z-z_o)^2}{4\alpha t}} \left[\begin{array}{l} erf\left(\frac{x+l}{2\sqrt{\alpha t}}\right) - erf\left(\frac{x+l_o}{2\sqrt{\alpha t}}\right) + \\ erf\left(\frac{x-l_o}{2\sqrt{\alpha t}}\right) - erf\left(\frac{x-l}{2\sqrt{\alpha t}}\right) \end{array}\right] \tag{10}$$

After a change in variable, Equation 10 can also be written as:

$$\Delta T_W = \frac{J_W}{4\pi kLM} \int_{\frac{1}{2\sqrt{\alpha t}}}^{\infty} \frac{d\tau}{\tau} \sum_{m=1}^{M} e^{-\left[(y-y(m))^2+(z-z_o)^2\right]\tau^2} \begin{bmatrix} erf\{(x+l)\tau\} - erf\{(x+l_o)\tau\} + \\ erf\{(x-l_o)\tau\} - erf\{(x-l)\tau\} \end{bmatrix} \tag{11}$$

where J_W is the average of the total power output from the wing heaters and L is the length of a wing heater. Similar to Equation (7), the integral in Equation (11) can be evaluated numerically. Combining Equations (1), (7), and (11), we finally obtain an expression for temperature rise at any location (x, y, z):

$$\Delta T(x, y, z, t) = \frac{J_H}{4\pi kH} \int_{\frac{1}{2\sqrt{\alpha t}}}^{\infty} \left[erf(y\tau) + erf\{(H-y)\tau\}\right] I_0\left[2rr_o\tau^2\right] e^{-(r^2+r_o^2)\tau^2} \frac{d\tau}{\tau} + \frac{J_W}{4\pi kLM} \int_{\frac{1}{2\sqrt{\alpha t}}}^{\infty} \frac{d\tau}{\tau} \sum_{m=1}^{M} e^{-\left[(y-y(m))^2+(z-z_o)^2\right]\tau^2} \begin{bmatrix} erf\{(x+l)\tau\} - erf\{(x+l_o)\tau\} + \\ erf\{(x-l_o)\tau\} - erf\{(x-l)\tau\} \end{bmatrix} \tag{12}$$

Equation 12 is the working equation for the remainder of the analysis in this paper.

From Equation 12, it is clear that the temperature rise at any location at a specified time has a nonlinear dependency on k and α. To obtain k and α from the temperature data at the DST, we adopt the following approach. We first take the temperature data at a particular time. We then subtract the preheat temperature data from those temperature data to obtain the temperature rise during a particular interval of time. Equation (12) was then fitted to these temperature-rise data using a nonlinear fitting routine with k and α as the fitting parameters. The nonlinear fitting routine uses the Gauss-Newton [*Gauss*, 1821] algorithm with Levenberg-Marquardt [*Levenberg*, 1944; *Marquardt*, 1963] modifications for global convergence. That is, it finds the parameter values for k and α that minimize the sum of the squared differences between the observed temperature rise data at any sensor location, and those calculated using Equation (12) at the same location at any specified time. With the host rock in the DST displaying two distinct states (not considering the two-phase zone), namely the wet and dry states, we will now apply our methodology to estimate k and α for both these states.

5. Results

The boiling temperature of the pore water is estimated to be 96–97°C under ambient pressure conditions in the subsurface of Yucca Mountain. This is further confirmed by the existence of the extended heat-pipe signature close to that temperature in the DST data (see, as an example, Figure 3b). For the purposes of our analysis, we will assume that the rock at any location is dry if the temperature is equal to or more than 100°C. In other words, it is assumed that all the water from the pore spaces has been boiled away by the time the temperature exceeds 100°C. On the other hand, we will assume a rock to be

in a wet condition if the temperature is equal to or below 95°C. This last assumption implies that large-scale boiling at the DST begins only above that temperature.

The parameters that have a considerable impact on temperature rise are the heating powers, J_H and J_W. That the DST was a field-scale open heater test has its inherent weaknesses, including the unmeasured heat losses from the test. Still, even in the absence of any heat loss, it is not possible to know precisely how much of the total input power was utilized in heating the rock and how much went into providing latent heat of phase change. Based on elaborate TH simulations of the DST using the TOUGH2 [*Pruess*, 1991] integral, finite-difference simulator, *Mukhopadhyay and Tsang* [2003] showed that about 74–81% of the total input power went into heating rock during first 27 months of heating. In Table 2, we show the estimated power utilized in heating rock at the DST through the entire heating phase. Table 2 is a continuation of the results presented in *Mukhopadhyay and Tsang* [2003]. In the absence of any concrete data, we will use these numbers as the total heat input in the system. In the following two subsections, we present our estimates of the dry and wet thermal conductivities, based on the total input power in Table 2. In Section 5.3, we will present results from a sensitivity analysis with input power as the variable.

5.1 Dry Thermal Properties

The boundaries of the dry and wet zones in the DST change dynamically with the progress of heating. At initial phases of heating, there is no dry zone. As heating continues, a small dry zone is formed near the HD and along the wing heaters. With further heating, the dry zone continues to expand, pushing the wet zone farther and farther away from the heat source. As an example, see the radial location of the boundary of the dry zone as recorded by the sensors in Boreholes 137, 138, and 139 at various times (Table 3). These three boreholes are representative samples of the data in the DST host rock, with Borehole 137 oriented vertically upwards, Borehole 138 oriented upwards at an angle of 45° with the HD, and Borehole 139 oriented horizontally. In Table 3, the distances are listed as those from the center of the HD. For example, at 12 months of heating, the boundary of the dry zone is located at 3.81 m in Borehole 137, 4.52 m in Borehole 138, and 13.4 m in Borehole 139 as measured from the center of the HD. This implies that, at 12 months of heating, any location closer than 3.81 m along Borehole 137 is recording a temperature of more than 100°C. By 24 months of heating, the dryout zone has expanded to 5.3 m in Borehole 137, 6.61 m in Borehole 138, and 14.3 m in Borehole 139. Towards the end of the heating phase at the DST (at 48 months), the dryout zone is located at 7.4 m, 9.02 m, and 15.5 m in Boreholes 137, 138, 139, respectively.

Because of this dynamically changing location of the dryout zone boundary, the analytical solution in Equation (12) has to be applied over different spatial extents at different times in order to obtain estimates of the dry thermal conductivities. For example, at 24 months of heating, we need to consider temperature data from sensors located at 5.3 m or closer from the HD in Borehole 137. For estimating the thermal properties of the dry state, we consider temperature data from the DST at 30, 36, 42 and 48 months of heating. The extent of the dryout zone was somewhat limited earlier than 30

months. Temperature data earlier than 30 months were thus not considered for the estimation of dry thermal properties. In Figures 5a and 5b, we show the measured temperatures in Boreholes 137, 138, and 139, along with the 'best fit' estimates of the calculated temperatures, at 36 and 48 months of heating. In Table 4, we provide the parameter values for k and α in the dry rock that produce the best fit with measured temperatures at various times. As a measure of goodness of fit, we provide the 95% confidence interval for both those parameters. It is seen that the estimated dry thermal conductivity value (1.43–1.49 W/m-K) is consistent with the estimation (mean of 1.45 W/m-K for Tptpmn) of Ramsey et al. (2002) through elaborate geostatistical simulation. This in turn validates our approach of estimating thermal conductivity from temperature data. In addition, our estimate was obtained with much less computational effort compared to that of Ramsey et al. (2002). Our estimate of the dry thermal conductivity is, however, somewhat different from that used in earlier TH modeling of the DST (*Birkholzer and Tsang*, 2000; *Mukhopadhyay and Tsang*, 2003), which was 1.67 W/m-K. This variance indicates the difference between a spot estimate (based on a core sample) from a certain location and a mean for the entire location.

5.2 Wet Thermal Properties

Before start of heating, the entire domain of the host rock can be considered as wet rock. With constant heating, as the dryout zone expands with continuous boiling of pore water, the wet zone is pushed away from the heat source. The inner boundary of the wet zone, located at the HD at the beginning of heating, moves away from the HD (the outer boundary of the wet zone remains at infinity, or at the end of the instrumentation boreholes for our purposes). In Table 5, we show the location of the inner boundary of the wet zone at various times. Recollect that we have defined the wet zone as any sensor location recording 95^{o}C or lower. The inner boundary of the wet zone is thus the contour of a 95^{o}C temperature. For example, in Borehole 137, the inner boundary of the wet zone can be found at a radial location of 7.4 m and 10.39 m at 24 months and 48 months of heating, respectively. At those same times, the 95^{o}C contours were located at 15.79 m and 17.59 m, respectively, in Borehole 139. The point we are trying to establish is that the extent of the wet zone is different in different boreholes at diferent times.

In Figure 6a, we show measured temperature increases in Boreholes 137–139 within the wet zone, i.e., wherever temperature was below 95^{o}C at 12 months of heating. In the same figure, we also show the computed temperature increases in those boreholes using the best-fit parameters for the wet zone. Figure 6b is similar to Figure 6a, except that the results are shown at 24 months of heating. In Table 6, the estimated parameter values are tabulated along with 95% confidence intervals for those parameters at various times. Observe that the estimated wet thermal conductivity is in the range 2.07–2.15 (W/m-K), except at six months when the estimated wet thermal conductivity is about 1.95 (W/m-K). Barring that anomaly, it appears that a reasonable estimate of wet thermal conductivity is 2.1 (W/m-K). This is again similar to the mean wet thermal conductivity value of 2.13 W/m-K for Tptpmn reported by Ramsey et al. (2002). This estimate is slightly different from the wet thermal conductivity of 2.0 W/m-K used in earlier analyses (*Birkholzer and Tsang*, 2000; *Mukhopadhyay and Tsang*, 2003).

5.3 Sensitivity Analysis

Temperature rise in the host rock of the DST is dependent upon the total heat utilized for heating the rock. Since there is some uncertainty exists (primarily due to heat losses) in determining what fraction of the input heat is actually used for heating the rock, uncertainties exist in the estimated (dry and wet) thermal conductivity values. In this section, we present some results to demonstrate the sensitivity of the estimated thermal conductivity values to uncertainty in the heat used for heating the rock.

Based on TOUGH2 simulation estimates (Table 2), 77.6% of the input heat was used in heating rock at 6 months of heating. It gradually decreased to 73.6% at 48 months of heating (close to the end of the heating phase). The gradual decrease in the fraction of input heat going into heating rock results from a larger fraction of heat being used in boiling water with the progress of heating. When very little boiling is taking place, say, during the first two to three months of heating, an even higher fraction (~81%) of input heat went into heating rock (*Mukhopadhyay and Tsang*, 2003). Thus, the maximum fraction (81%) of input heat used for heating rock is about 10% higher than the minimum fraction (73.6% at 48 months) of heat used for that purpose. This represents an uncertainty range for the total heat to be used in calculating the thermal conductivities. It was thus decided to a perform sensitivity analysis with heat input into our model as ±5% of those listed in Table 2 at any given time.

Table 7 shows estimated best-fit dry thermal conductivity values at various times with different heat inputs. The second column in Table 7 shows the best-fit dry thermal conductivity with 95% of the heat shown in Table 2, whereas the fourth column shows the same with 105% of the heat shown in Table 2. The third column is reproduced from Table 4 for easy comparison. Similarly, Table 8 shows the best-fit wet thermal conductivities at various times. From Tables 7 and 8, it is evident that reducing the heat input by 5% results in almost a 5% reduction in the estimated thermal conductivity values. Similarly, increasing the heat input by 5% results in a similar increase in the estimated thermal conductivity values. This almost linear dependency is expected (see Equation [12]). Also, changing the heat input does not impact the estimate of thermal diffusivity (this observation is also borne out of Equation [12]). The estimated dry and thermal conductivity values (after varying the heat input) are not dissimilar to the 95% confidence interval around the best-fit obtained using the heat listed in Table 2 as input to our model. It thus can be concluded that, even after assuming a 10% uncertainty in estimating the heat used for raising the temperature in the DST host rock, the temperature data produce a consistent estimate of thermal conductivity. Since these estimates have been obtained using actual temperature data from the DST over a wide spatial and temporal range, they possibly represent the true mean thermal conductivities of the host rock (as opposed to spot observation through core measurements). The validity of the present estimates is further confirmed by the observation of Ramsey et al. (2002) through elaborate geostatistical simulations. However, the simplicity of the underlying concept presented in this paper ensures that no elaborate geostatistical simulations are needed to obtain the same results.

6. Summary

The large volume of temperature data collected from the DST provides an opportunity to estimate the field-scale thermal conductivity of the host rock. A field-scale estimate of the thermal conductivity is expected to be more reliable than that from core measurements in predicting the TH conditions likely to evolve in the host rock of the repository. In previous modeling studies of the TH conditions resulting from heating in the DST, thermal conductivity values from core measurements have been used as input. While these measured thermal conductivity values were adequate as starting points for modeling activities, they did not represent the true large-scale thermal conductivities of the host rock. Ramsey et al. (2002) realized this problem and performed elaborate geostatistical simulations to obtain an estimate of field-scale thermal conductivity of the host rock. However, these geostatistical simulations are computationally very intensive. Also, these simulations use the core measurements as input for obtaining field-scale thermal conductivity. Thus, their results are not independent estimates of the field-scale thermal conductivities.

In this paper, we provide an efficient methodology for estimating the field-scale thermal conductivities of the host rock. This proposed method requires no elaborate statistical simulations. Additionally, this method derives the thermal conductivities from actual temperature data collected over large spatial and temporal scale and does not use the core measurements as input. As a result, these newly estimated thermal conductivity values can be used as independent verification of the previous estimates.

The thermal regime in the DST host rock can be described in terms of "wet" and "dry" zones. At the beginning of heating, the entire host rock was about 90% saturated with water and could be called "wet". With progress of heating, as water started boiling, a dryout zone appeared, and expanded with further heating. At the end of heating, although the wet zone was still present, there was a considerable dryout zone near the HD. Temperature data from the DST clearly established these wet and dry zones (including a two-phase zone as well). Temperature data also established the fact that thermal conductivities were different in the dry and wet zones.

We have developed an analytical solution for transient temperature rise in the DST host rock. This analytical solution has two components: rise in temperature caused by heat emanating from the canister heaters and that caused by heat coming from the wing heaters. This analytical solution was then separately fitted to measured temperatures in the dry and wet zones at various times of data collection. We report the best-fit estimates from the exercise as the field-scale thermal conductivity for the dry and wet rock. We also provide the 95% confidence level for our estimates. As expected, our field-scale estimates are different from raw core measurement values (*Brodsky et al*., 1997) and are more consistent with the findings of Ramsey et al. (2002). However, our estimates were obtained with much less computational effort.

A likely source of uncertainty in our estimates is the amount of heat actually used in heating the rock. Detailed modeling of the TH conditions in the DST host rock has indicated that at least 73.6% (and at a maximum 81%) of the heat has been utilized in heating the rock. As a sensitivity analysis, we obtained the range of thermal condutivity (both dry and wet) that would result from a 10% uncertainty in input heat. The range is within the 95% confidence limit of the best estimates.

Nomenclature

C Specific heat capacity, J/kg-K.
H Length of the HD, m.
J_H Average of total power from the HD, W.
J_W Average of total power from the wing heaters, W.
k Thermal conductivity, W/m-K.
k_d Dry thermal conductivity, W/m-K.
k_w Wet thermal conductivity, W/m-K.
l x-coordinate of the end of the wing heater, m.
l_o x-coordinate of the start of the wing heater, m.
L Length of a wing heater, m.
M Pairs of wing heaters.
Q Strength of point source of heat, m^3-K.
r Radial location, m.
r_o Radius of the HD, m.
ΔT Total temperature rise, ^oC.
ΔT_H Temperature rise due to heat coming from the HD, ^oC.
ΔT_W Temperature rise due to heat coming from the wing heaters, ^oC.
t time, s.
t_o time, s.
x x-coordinate, m
y y-coordinate, m
z z-coordinate, m
x_o x-coordinate of point source of heat, m.
y_o y-coordinate of point source of heat, m.
z_o z-coordinate of point source of heat, m.
α Thermal diffusivity, m^2/s.
ρ Density, kg/m^3

Acknowledgments. We thank the anonymous reviewers of the WRR for their careful and critical review of the manuscript. We thank Yu-Shu Yu, Nicolas Spycher, and Dan Hawkes of the Ernest Orlando Lawrence Berkeley National Laboratory (Berkeley Lab) for their constructive review of the draft manuscript. This work was supported by the Director, Office of Civilian Radioactive Waste Management, U.S. Department of Energy, through Memorandum Purchase Order EA9013MC5X between Bechtel SAIC Company, LLC, and Berkeley Lab. The support is provided to Berkeley Lab through the U.S. Department of Energy Contract No. DE-AC03-76SF00098.

References

Abramowitz, M. and Stegun, I. A. (eds.), *Handbook of Mathematical Functions*, National Bureau of Standards, Washington, D.C., 1964.

Bandurraga, T. M. and Bodvarsson, G. S., Calibrating hydrogeologic properties for the 3-D site scale unsaturated model of Yucca Mountain, Nevada, *Journal of Contaminant Hydrology*, **38** (1-3), 25-46, 1999.

Birkholzer, J. T. and Tsang, Y. W., Pretest analysis of the thermal-hydrological conditions of the ESF Drift Scale Test, *Rep. LBNL-41044*, Lawrence Berkeley National Laboratory, Berkeley, CA, 1997.

Birkholzer, J.T. and Tsang, Y.W., Modeling the thermal-hydrologic processes in a large-scale underground heater test in partially saturated fractured tuff, *Water Resources Research*, **36** (*6*), 1431-1447, 2000.

Birkholzer, J.T., Mukhopadhayay, S., and Tsang, Y. W., *Drift-Scale Coupled Processes (DST and TH Seepage) Models*, MDL-NBS-HS-000015 REV00, BSC, Las Vegas, NV, 2003.

Brodsky, N. S., Riggins, M., Connolly, J., and Ricci, P., *Thermal expansion, thermal conductivity, and heat capacity measurements for boreholes UE25 NRG-4, UE25 NRG-5, USW NRG-6, and USW NRG-7/7A*, SAND95-1955 UC-814, Sandia National Laboratory, Albuquerque, NM, 1997.

Carslaw, H. S. and Jaeger, J. C., *Conduction of Heat in Solids*, Oxford University Press, New York, NY, 1959.

CRWMS, *Drift Scale Test As-Built Report*, BAB000000-01717-5700-00003 REV 01, CRWMS M&O, Las Vegas, NV, 1998.

CRWMS, *Thermal Tests Thermal-Hydrological Analyses/Model Report*, ANL-NBS-TH-000001 REV 00, CRWMS M&O, Las Vegas, NV, 2000.

Finsterle, S., *ITOUGH2 User's Guide*, LBNL-40040 UC 400, Lawrence Berkeley National Laboratory, Berkeley, CA, 1999.

Gauss, C. F., *Theoria Combinationis Observationum Erroribus Minimis Obnoxiae, pars prior*, 1821, translated by G. W. Stewart, *Theory of the Combination of Observations Least Subject to Errors*, Society of Industrial and Applied Mathematics, Philadelphia, PA, 1995.

Hsu, C. T., Cheng, P., and Wong, K. W., A lumped-parameter model for stagnant thermal conductivity of spatially periodic porous media, *Journal of Heat Transfer*, **117** (2), 264-269, 1995.

Levenberg, K., A method for the solution of certain nonlinear problem in least squares, *Quart. Appl. Math*., **2**, 164-168, 1944.

Marquardt, D. W., An algorithm for least squares estimation of nonlinear parameters, *SIAM J. Appl. Math*., **11**, 431-441, 1963.

Mukhopadhyay, S. and Tsang, Y. W., Uncertainties in coupled thermal-hydrological processes associated with the Drift Scale Test at Yucca Mountain, Nevada, *Journal of Contaminant Hydrology*, **62-63**, 595-612, 2003.

Pruess, K., TOUGH2 User's Guide, *Technical Report LBL-20700*, E. O. Lawrence Berkeley National Laboratory, Berkeley, CA, 1987.

Ramsey, J., Bean, J., Lum, C., and Harding, E., *Conductivity of the Potential Repository Horizon*, MDL-NBS-GS-000005 REV00, BSC, Las Vegas, NV, 2003.

Tsang, Y. W., Birkholzer, J. T., Freifeld, B., Peterson, J., Hu, M. Q., Sonnenthal, E., and Spycher, N., Yucca Mountain single heater test final report, *Rep. LBNL-42537*, Lawrence Berkeley National Laboratory, Berkeley, CA, 1999.

S. Mukhopadhyay, Ernest Orlando Lawrence Berkeley National Laboratory, MS 90-1116, 1 Cyclotron Road, Berkeley, CA 94720 (Smukhopadhyay@lbl.gov)

Y.W. Tsang, Ernest Orlando Lawrence Berkeley National Laboratory, MS 90-1116, 1 Cyclotron Road, Berkeley, CA 94720 (YTTsang@lbl.gov).

Table Captions

Table 1. Average input power at the Drift Scale Test at various times

Table 2. Estimated [*Mukhopadhyay and Tsang*, 2003] power for heating rock at various times

Table 3. Radial location of measured 100°C temperature contours in Boreholes 137, 138, and 139

Table 4. Estimated dry thermal properties of the fractured welded tuff of Tptpmn at Yucca Mountain, Nevada

Figure Captions

Table 1

Time (months)	Average of Total Canister Heater Power	Average of Total Wing Heater Power	Average of Total Heating Power

	(kW)	(kW)	(kW)
6	51.67	134.70	186.37
12	52.09	133.26	185.35
18	52.07	132.15	184.22
24	51.43	129.86	181.29
30	50.96	128.65	179.61
36	49.86	125.62	175.48
42	48.76	122.36	171.12
48	47.70	119.43	167.13

Table 2

Time (months)	Average of Total Heating Power (kW)	Estimated Power for Heating Rock[1] (kW)	% of Input Power in Heating Rock
6	186.37	144.7	77.6
12	185.35	139.0	75.0

[1] From TOUGH2 simulations of the DST [*Mukhopadhyay and Tsang*, 2003]

18	184.22	137.8	74.8
24	181.29	135.4	74.7
30	179.61	133.3	74.2
36	175.48	129.6	73.9
42	171.12	126.5	73.9
48	167.13	123.1	73.6

Table 3

Time (months)	Radial Distance of 100°C Contours from the Center of the HD (m)		
	Borehole 137	Borehole 138	Borehole 139
6	2.91	3.32	12.2
12	3.81	4.52	13.4
18	4.71	6.32	14.0
24	5.30	6.61	14.3
30	5.90	7.82	14.9
36	6.50	8.42	15.2
42	7.10	8.72	15.2
48	7.40	9.02	15.5

Table 4

Time (months)	Estimated Parameter Values for dry conditions	
	Dry Thermal Conductivity, k_d (W/m-K)	Thermal Diffusivity, α (m^2/s)

	Best Fit	95% Confidence Interval	Best Fit	95% Confidence Interval
30	1.49	1.41-1.57	0.3609×10^{-6}	0.3312×10^{-6}—0.3944×10^{-6}
36	1.46	1.39-1.53	0.3717×10^{-6}	0.3386×10^{-6}—0.4067×10^{-6}
42	1.43	1.37-1.49	0.3907×10^{-6}	0.3582×10^{-6}—0.4232×10^{-6}
48	1.48	1.42-1.55	0.3883×10^{-6}	0.3540×10^{-6}—0.4226×10^{-6}

Table 5

Time (months)	Radial Distance of 95°C Contours from the Center of the HD (m)		
	Borehole 137	Borehole 138	Borehole 139
6	3.51	3.92	13.40
12	4.71	5.41	14.60
18	5.60	7.22	15.20
24	7.40	9.01	15.79
30	8.30	9.62	16.39
36	8.90	10.83	16.99
42	9.79	12.03	16.99
48	10.39	12.34	17.59

Table 6

Time (months)	Estimated Parameter Values for wet conditions			
	Thermal Conductivity, k (W/m-K)		Thermal Diffusivity, α (m^2/s)	
	Best Fit	95% Confidence Interval	Best Fit	95% Confidence Interval

6	1.95	1.87-2.03	1.0137×10^{-6}	0.9731×10^{-6}—1.0543×10^{-6}
12	2.09	2.01-2.17	1.0803x10-6	0.9832×10^{-6}—1.1775×10^{-6}
18	2.13	2.03-2.23	1.0382×10^{-6}	0.9547×10^{-6}—1.1212×10^{-6}
24	2.07	1.99-2.15	0.9754×10^{-6}	0.9076×10^{-6}—1.0431×10^{-6}
30	2.15	2.06-2.22	1.0457×10^{-6}	0.9564×10^{-6}—1.1350×10^{-6}
36	2.12	2.04-2.19	1.0567×10^{-6}	0.9727×10^{-6}—1.1408×10^{-6}
42	2.07	1.98-2.16	1.015×10^{-6}	0.9479×10^{-6}—1.0818×10^{-6}
48	2.08	2.00-2.14	1.0576×10^{-6}	0.9652×10^{-6}—1.1500×10^{-6}

Table 7

Time (months)	Best-fit Dry Thermal Conductivity (W/m-K)		
	0.95*Heat in Table 2	Heat in Table 2	1.05*Heat in Table 2
30	1.43	1.49	1.57
36	1.41	1.46	1.53

42	1.37	1.43	1.50
48	1.42	1.48	1.55

Table 8

Time (months)	Best-fit Wet Thermal Conductivity (W/m-K)		
	0.95*Heat in Table 2	Heat in Table 2	1.05*Heat in Table 2
6	1.87	1.95	2.05
12	2.00	2.09	2.18
18	2.03	2.13	2.22
24	1.98	2.07	2.18
30	2.04	2.15	2.24
36	2.02	2.12	2.20
42	1.99	2.07	2.16
48	1.99	2.08	2.17

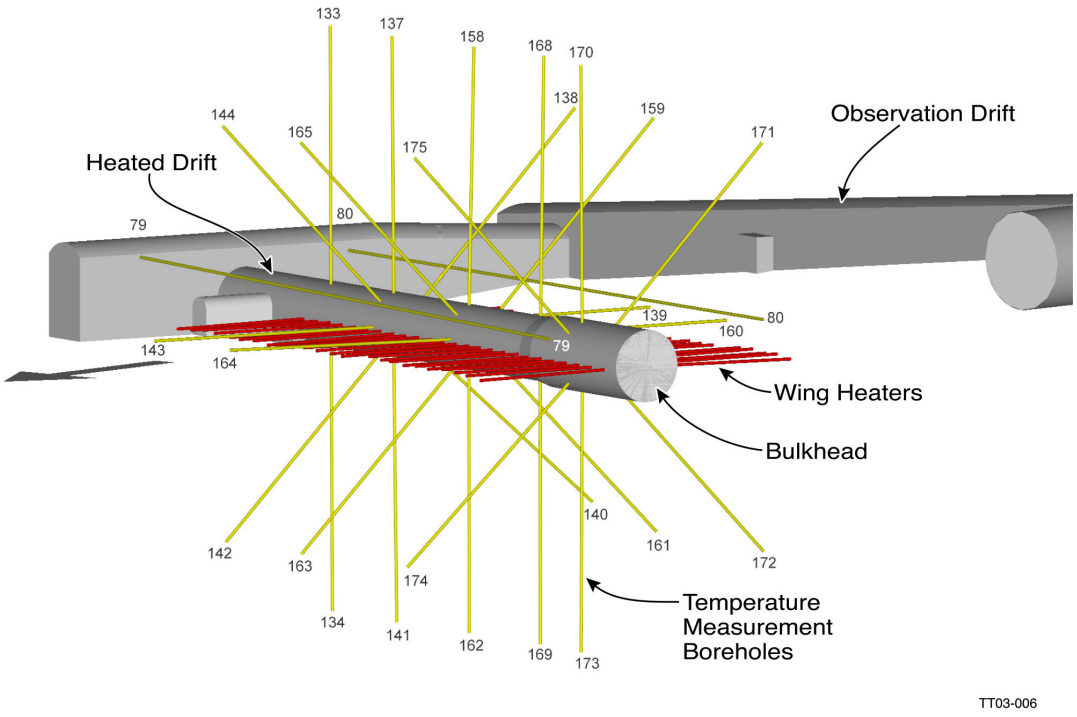
133
137
158
168
170
138
159
144
165
175
171
Observation Drift
Heated Drift
79
80
139
160
80
143
164
79
Wing Heaters
Bulkhead
140
142
163
161
172
174
Temperature
Measurement
Boreholes
134
141
162
169
173
TT03-006

Figure 1

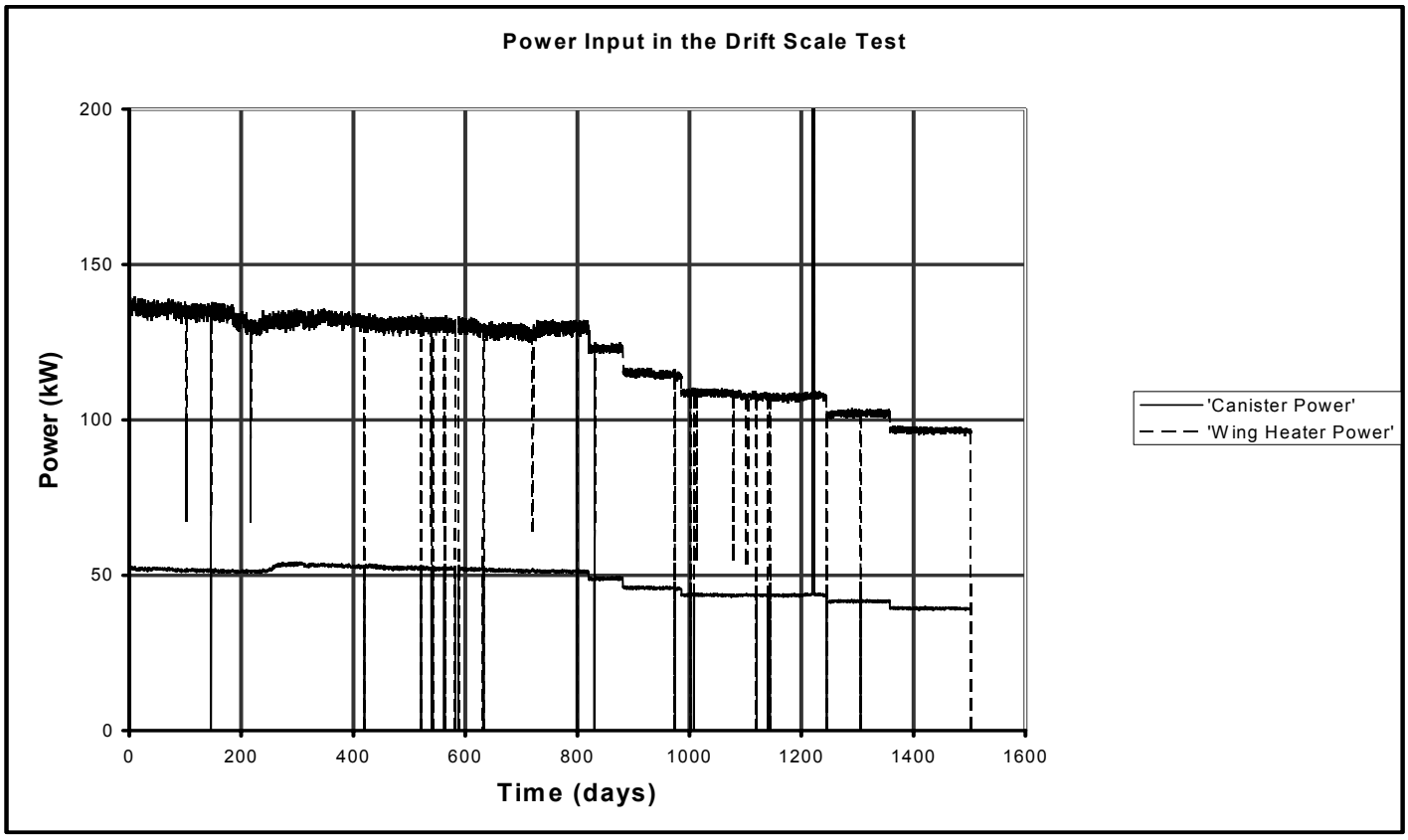
Power Input in the Drift Scale Test
Power (kW)
200
150
100
50
0
0
200
400
600
800
1000
1200
1400
1600
Time (days)
'Canister Power'
'Wing Heater Power'

Figure 2.

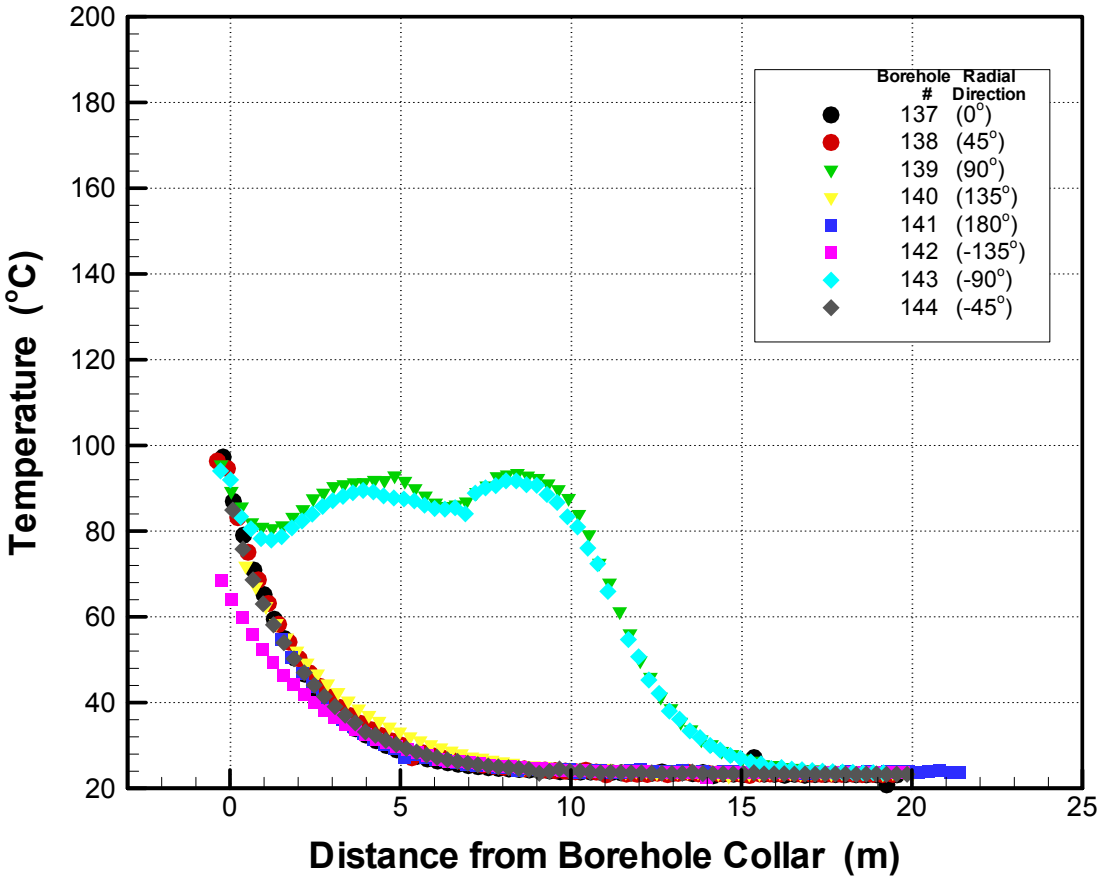
Temperature (°C)
Distance from Borehole Collar (m)
Borehole # Radial Direction
137 (0°)
138 (45°)
139 (90°)
140 (135°)
141 (180°)
142 (-135°)
143 (-90°)
144 (-45°)
200
180
160
140
120
100
80
60
40
20
0
5
10
15
20
25

Figure 3a

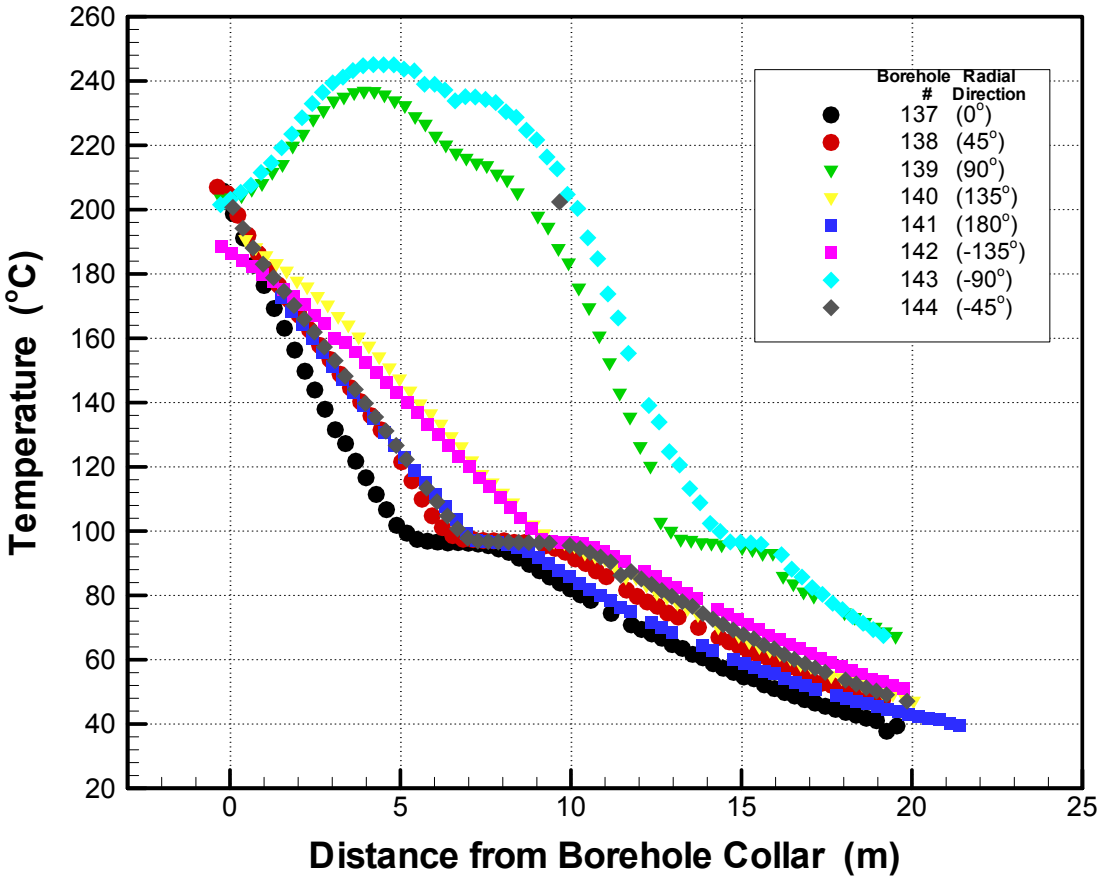
Temperature (°C)
Distance from Borehole Collar (m)
Borehole # Radial Direction
137 (0°)
138 (45°)
139 (90°)
140 (135°)
141 (180°)
142 (-135°)
143 (-90°)
144 (-45°)

Figure 3b.

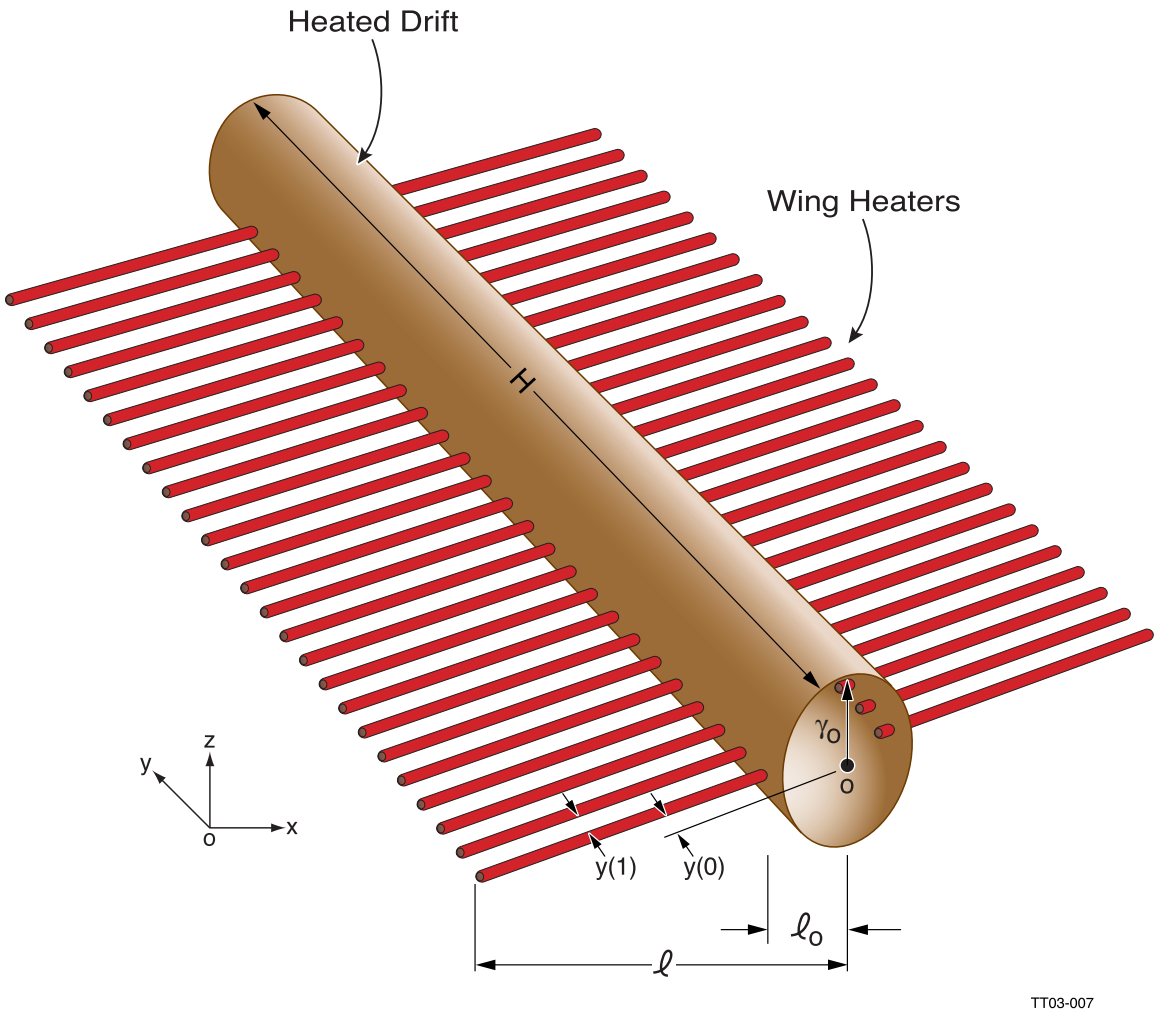
Heated Drift
Wing Heaters
H
z
y
o
x
γ_o
o
y(1)
y(0)
ℓ_o
ℓ
TT03-007

Figure 4

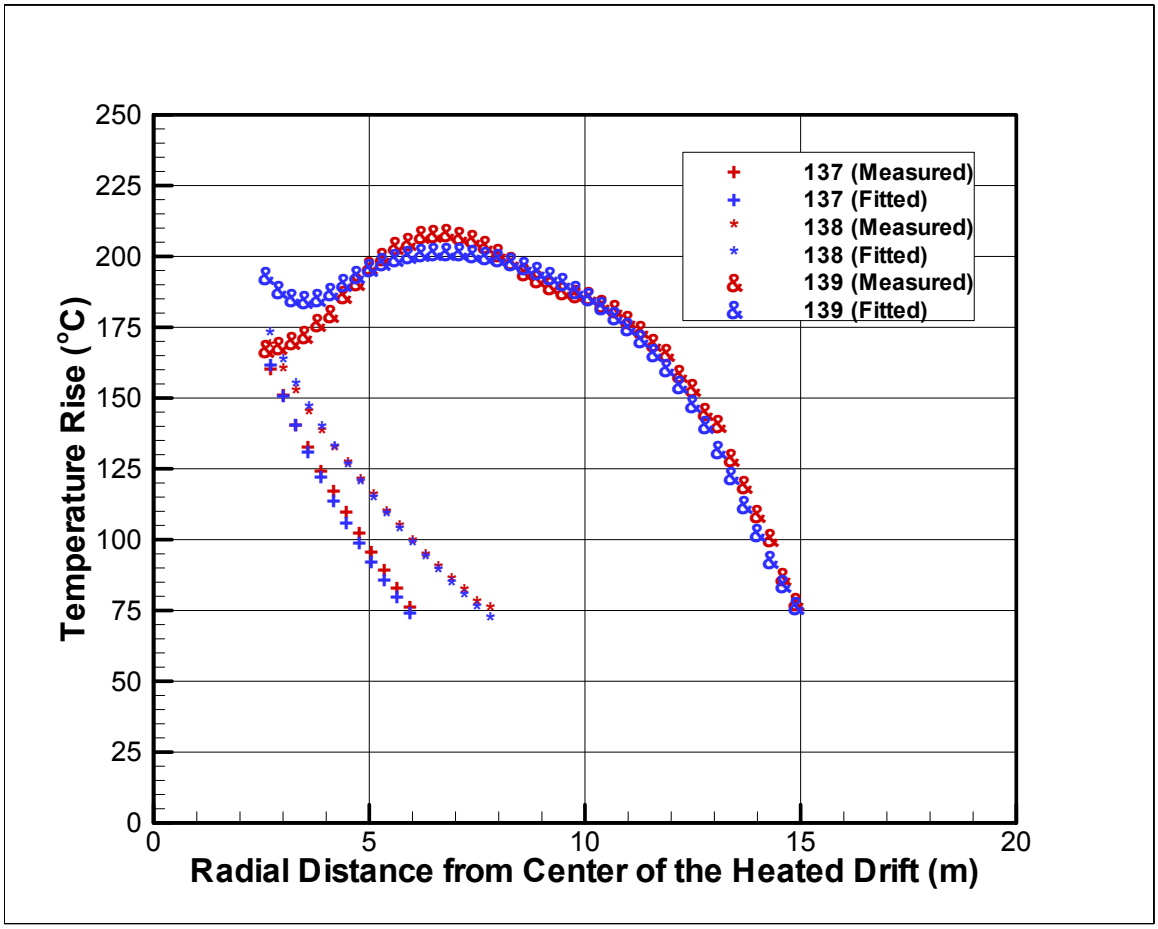
Temperature Rise (°C)
Radial Distance from Center of the Heated Drift (m)
137 (Measured)
137 (Fitted)
138 (Measured)
138 (Fitted)
139 (Measured)
139 (Fitted)
0
25
50
75
100
125
150
175
200
225
250
0
5
10
15
20
Figure 5a

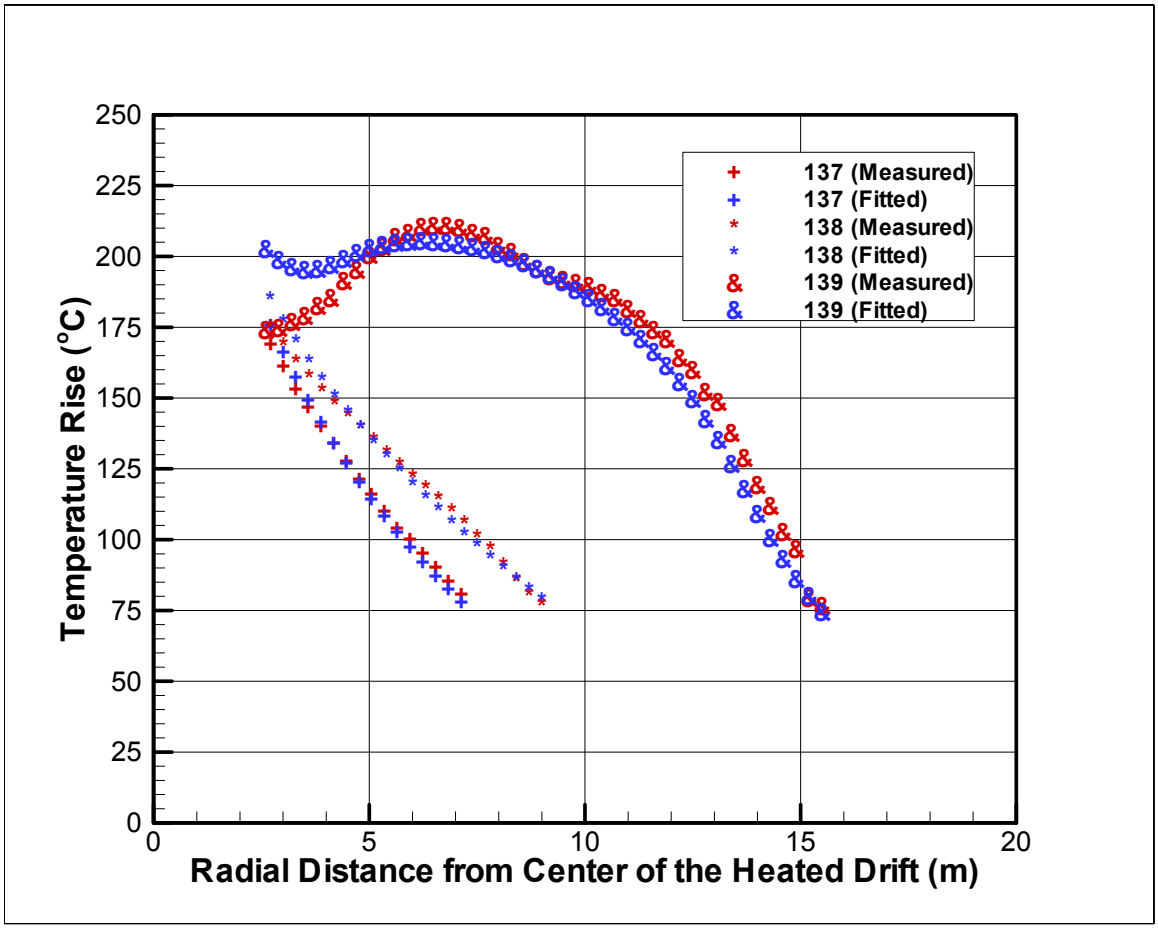
Temperature Rise (°C)
Radial Distance from Center of the Heated Drift (m)
137 (Measured)
137 (Fitted)
138 (Measured)
138 (Fitted)
139 (Measured)
139 (Fitted)
0
25
50
75
100
125
150
175
200
225
250
0
5
10
15
20
Figure 5b

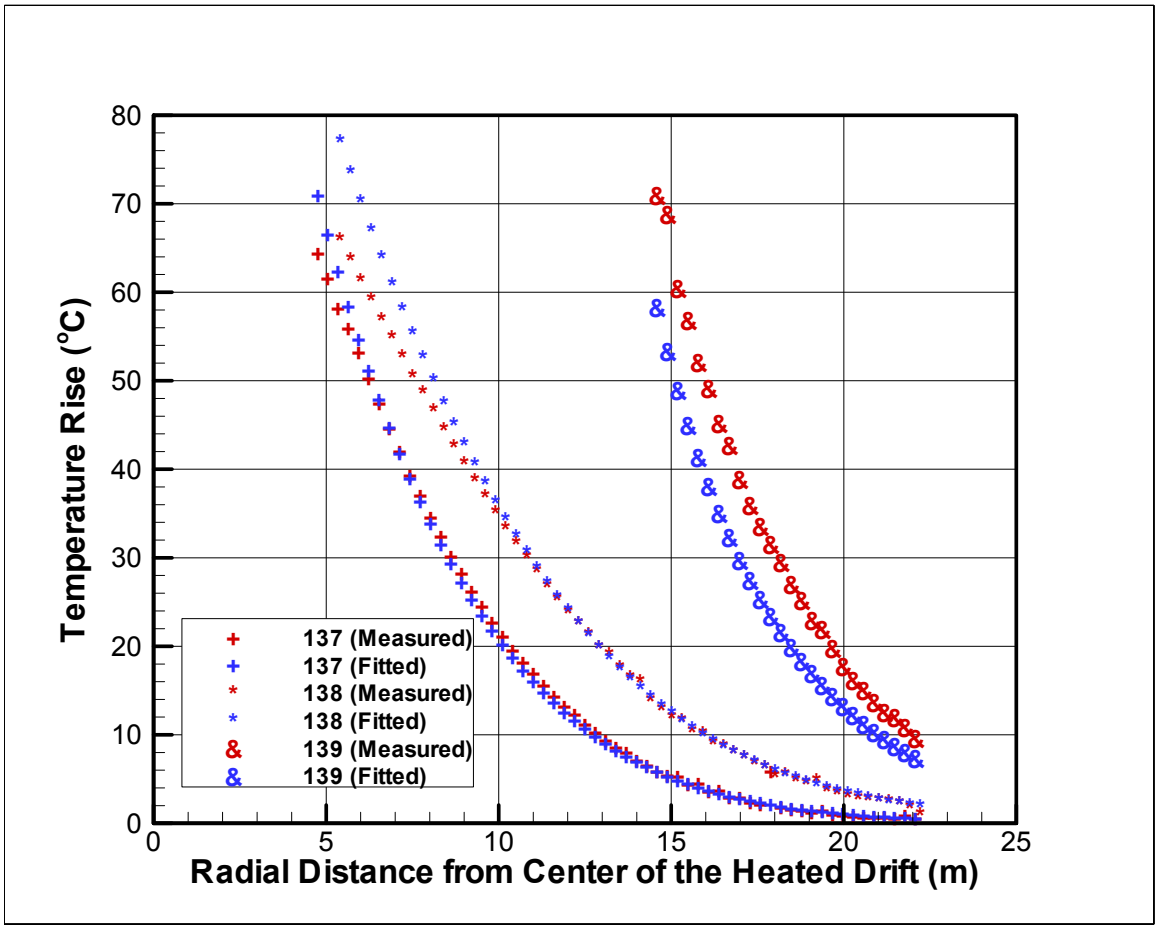
Temperature Rise (°C)
Radial Distance from Center of the Heated Drift (m)
0
10
20
30
40
50
60
70
80
0
5
10
15
20
25
137 (Measured)
137 (Fitted)
138 (Measured)
138 (Fitted)
139 (Measured)
139 (Fitted)

Figure 6a

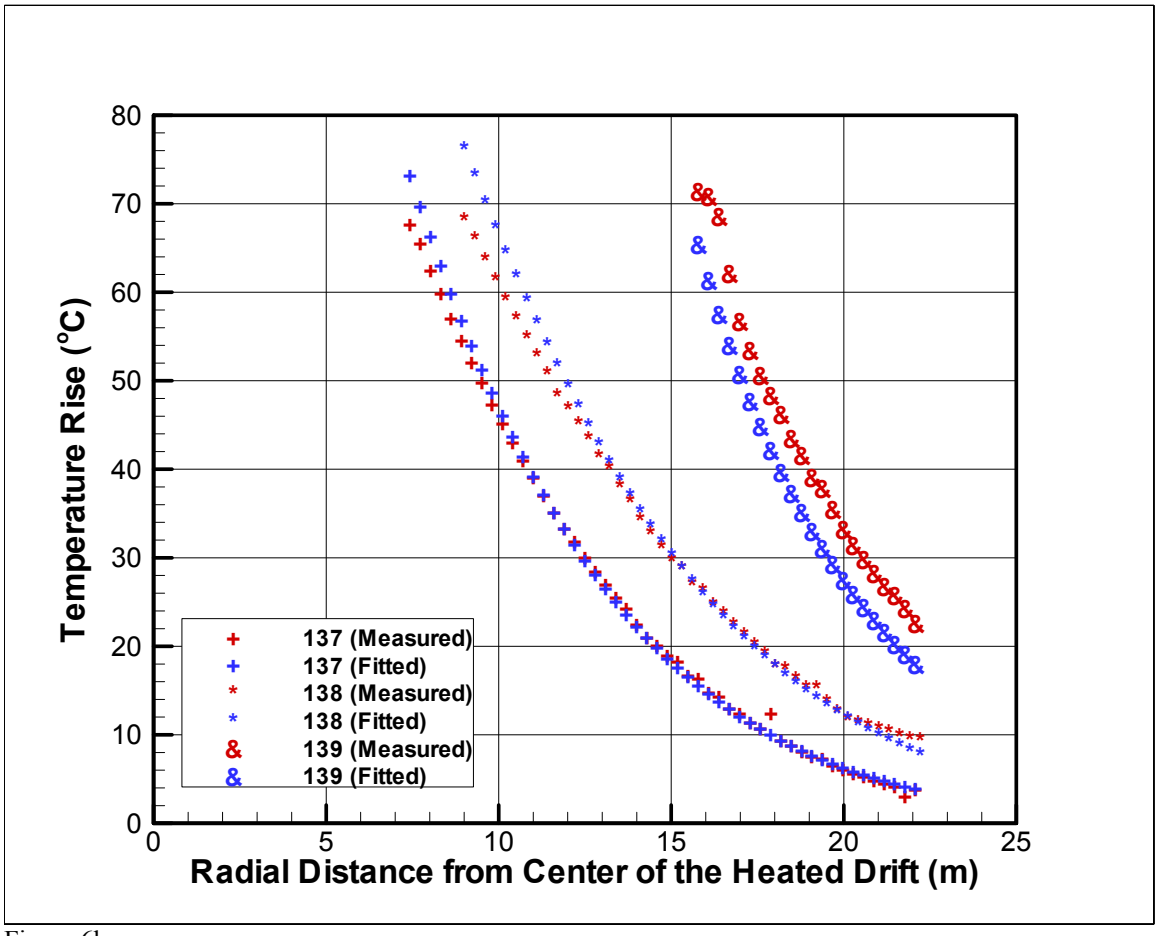
Temperature Rise (°C)
Radial Distance from Center of the Heated Drift (m)
0
10
20
30
40
50
60
70
80
0
5
10
15
20
25
137 (Measured)
137 (Fitted)
138 (Measured)
138 (Fitted)
139 (Measured)
139 (Fitted)
Figure 6b